ACS APPLIED MATERIALS & INTERFACES

www.acsami.org Research Article

Mechanistic Insight into Solution-Based Atomic Layer Deposition of CuSCN Provided by In Situ and Ex Situ Methods

Felix Hilpert,[⊥] Pei-Chun Liao,[⊥] Evanie Franz, Vanessa M. Koch, Lukas Fromm, Ece Topraksal, Andreas Görling, Ana-Sunčana Smith, Maïssa K. S. Barr, Julien Bachmann, Olaf Brummel,* and Jörg Libuda

Cite This: *ACS Appl. Mater. Interfaces* 2023, 15, 19536−19544 Read Online

ACCESS | Metrics & More | Article Recommendations | Supporting Information

ABSTRACT: Solution-based atomic layer deposition (sALD) processes enable the preparation of thin films on nanostructured surfaces while controlling the film thickness down to a monolayer and preserving the homogeneity of the film. In sALD, a similar operation principle as in gas-phase ALD is used, however, with a broader range of accessible materials and without requiring expensive vacuum equipment. In this work, a sALD process was developed to prepare CuSCN on a Si substrate using the precursors CuOAc and LiSCN. The film growth was studied by ex situ atomic force microscopy (AFM), analyzed by a neural network (NN) approach, ellipsometry, and a newly developed in situ infrared (IR) spectroscopy experiment in combination with density functional theory (DFT). In the self-limiting sALD process, CuSCN grows on top of an initially formed two-dimensional (2D) layer as three-dimensional spherical nanoparticles with an average size of ∼25 nm and a narrow particle size distribution. With increasing cycle number, the particle density increases and larger particles form via Ostwald ripening and coalescence. The film grows preferentially in the β-CuSCN phase. Additionally, a small fraction of the α-CuSCN phase and defect sites form.

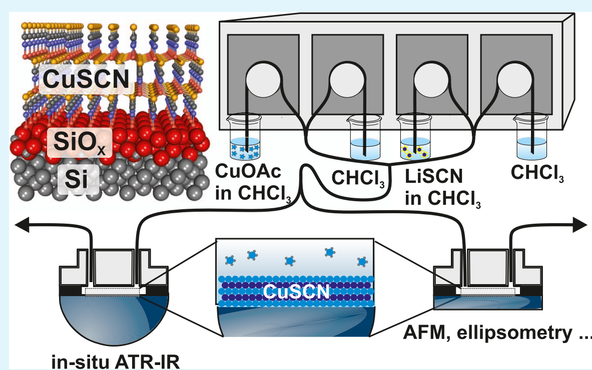

KEYWORDS: *solution atomic layer deposition, liquid phase, in situ IR spectroscopy, atomic force microscopy, copper thiocyanate, neural network, density functional theory, liquid atomic layer deposition*

Downloaded via FRIEDRICH-ALEXANDER-UNIV on June 7, 2023 at 13:58:12 (UTC).
See https://pubs.acs.org/sharingguidelines for options on how to legitimately share published articles.

INTRODUCTION

Miniaturization in semiconductor industries requires processes that enable the preparation of uniform thin films on nanostructured surfaces controlling precisely the film thickness and conformality. A method that fulfills all of these requirements is atomic layer deposition (ALD),[1,2] in earlier work also called atomic layer epitaxy (ALE) pioneered by Kol'tsov and Suntola.[3−11] An ALD process consists of the repetition of at least two complementary self-limiting surface reactions performed sequentially. Between the different reaction steps, the precursor is removed by purging or pumping. This procedure enables to grow extremely smooth layers ideally with monolayer precision, which are conformal to the original substrate.[1,2] Conventional ALD is a gas-phase process (gALD), which comes, however, with several disadvantages. First, the number of available precursors in gALD is limited. The precursors have to be highly reactive yet robust enough so that they do not decompose thermally. Further, the majority of ALD processes in the gas phase require vacuum conditions, which involve costly equipment.[12,13] These limitations can be overcome by transferring the ALD approach into the liquid phase,[14−24] the so-called solution ALD (sALD) or liquid ALD (LALD) process. The principle remains the same, namely, the ability to have self-limited growth behavior, even though the environment is different. The dilution of reactive species in an inert solvent broadens hereby the field of applicable precursors and there is no requirement for its high vapor pressure any longer. Some types of precursors, such as ionic compounds, cannot be processed at all by conventional ALD. Furthermore, the handling of liquids requires less complicated and less costly equipment and sALD processes can be operated at room temperature and ambient pressure, and therefore, any type of substrates can be used. Importantly, scientists can fall back on available knowledge and processes from solution chemistry, which opens a large toolbox of different sALD approaches, such as, e.g., the surface sol−gel (SSG) approach,[17,18,25] hydrolysis,[20,21] redox-layer deposition (RLD),[22,23] or electrochemical ALD (E-ALD).[26] The possibility to grow a layer in a self-limiting

Received: September 21, 2022
Accepted: March 6, 2023
Published: April 5, 2023

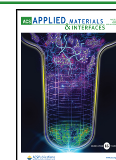

© 2023 American Chemical Society

https://doi.org/10.1021/acsami.2c16943
ACS Appl. Mater. Interfaces 2023, 15, 19536−19544

Table 1. Chemicals and Parameters Used in the sALD Process

name	description	supplier	concentration	flow rate [mL·s^{-1}]	flow time per cycle [s]	acquisition time[b] per cycle [s]	volume per cycle [mL]
reactant 1	CuOAc[a]	Sigma-Aldrich	saturated ∼ 1 mM	31.25	160	204	5
purge 1	$CHCl_3$	Sigma-Aldrich		150	240		36
reactant 2	LiSCN[a]	Sigma-Aldrich	saturated ∼ 1 mM	41.67	120	204	5
purge 2	$CHCl_3$	Sigma-Aldrich		150	240		36

[a]In $CHCl_3$. [b]Without flow.

process by sALD relies on a chemical reaction at the interface. The reaction is driven by the fact that the precursor reacts on the surface, forming an insoluble layer of the product. In contrast, the byproduct is soluble in the chosen solvent.

In recent years, research groups demonstrated the potential of sALD by the development of sALD processes for a variety of different materials.[27−30] It was shown that high conformity on high aspect ratio features can also be achieved by sALD.[19] To the best of our knowledge, however, no sALD process was developed for CuSCN so far. CuSCN is a p-type semiconductor with a wide band gap of ≥3.5 eV and is used, e.g., in photovoltaic applications. Note that for technical applications, CuSCN films are post-processed after deposition to optimize the physical properties.[31] The films can reach a high hole mobility, good thermal stability, and a work function well-aligned with some light absorber semiconductors of interest for photovoltaic applications.[32,33] It transmits light across the entire visible and near-infrared spectrum, making it attractive especially for tandem cell applications.[34] Certified power conversion efficiencies of perovskite solar cells greater than 20% and long-term stability (>95% of their initial efficiency after aging for 1000 h) have been realized using CuSCN as the hole extraction layer.[35] Moreover, solution-processed low-voltage flexible thin-film transistors have been developed based on CuSCN.[36] Among those solution processes, however, no one allows a precision at the atomic level. Further, no gas processes are available as thiocyanate is difficult to obtain in the vapor phase without changing the stoichiometry.

For sALD processes in general, there is still a lack of mechanistic understanding of the surface processes initiating the film growth. This limits further conceptual developments and optimization. In earlier work, mainly ex situ approaches were applied to study the growth mechanisms, such as the atomic force microscopy, ellipsometry, and X-ray reflectometry (XRR).[16,19,37] While in gALD, in situ methods contributed particularly to the mechanistic understanding,[12,38−42] these methods are rarely found for sALD. In this context, Stickney and co-workers studied in situ the growth of different nanofilms deposited by an E-ALD process using electrochemical scanning tunneling microscopy (EC-STM).[30,43]

In this work, a newly developed in situ IR approach is applied to study a new sALD growth process for deposition of CuSCN on SiO_x/Si. This experimental setup enables us to correlate the chemical nature during growth in solution with the structural information obtained by ex situ atomic force microscopy (AFM). The results demonstrate that nucleation, coalescence and/or ripening, and the formation of defect sites take place in the initial stages of the investigated sALD process. This finding shows the potential of the presented approach to provide insights into the mechanism of sALD processes.

EXPERIMENTAL AND THEORETICAL METHODS

Attenuated Total Reflection Infrared (ATR-IR) Experiments. *Cleaning of the Equipment*. All equipment made out of glass, Teflon, or Kalrez was stored in a solution of NOCHROMIX (Sigma-Aldrich) in concentrated sulfuric acid (Merck, Emsure, 98%) overnight. Prior to each measurement, the equipment was rinsed 15 times with ultrapure water (MilliQ Synergy UV, 18.2 MΩ·cm at 298 K, TOC < 5 ppb) and dried subsequently.

ATR-IR. All spectra were recorded using a Fourier transform infrared (FT-IR) spectrometer (Bruker, Vertex 80v) with evacuated beam path to obtain high sensitivity and stability. The spectrometer was equipped with a liquid-nitrogen-cooled mercury cadmium telluride (MCT) detector, a commercial optics for liquid cells (Bruker, A530/v), and a home-build flow cell to measure in ATR mode (see details below and in the Supporting Information). All spectra were recorded with 512 scans per spectrum, a scanner velocity of 40 kHz, and a resolution of 2 cm^{-1} leading to an acquisition time of 3 min 24 s per spectrum. The setup was equipped with a Si hemisphere (Korth, d = 25 mm) underneath, which serves as the ATR-IR window and as a substrate for the sALD process. The Si hemisphere was cleaned before each measurement by a freshly prepared piranha acid solution (H_2SO_4 (Merck, Emsure, 98%)/H_2O_2 (Merck, SAFC, 30%) in the ratio 2:1). Afterward, the window was rinsed with ultrapure water (MilliQ synergy UV, 18.2 MΩ·cm at 25 °C, <5 ppb TOC) thoroughly and dried in vacuum. The measurements were performed in ATR mode. As precursors, solutions of CuOAc (Sigma-Aldrich, 99.0%) and LiSCN (Sigma-Aldrich, 98.0−102.0% dry basis) in $CHCl_3$ (Sigma-Aldrich, anhydrous, >99.0%) were used. After each precursor, the cell was purged with $CHCl_3$ (Sigma-Aldrich, ≥99.8%). The reference transmission spectrum was recorded using CuSCN powder (Sigma-Aldrich, 99.0%) in KBr (Sigma-Aldrich, ≥99% trace metals basis) with 128 scans.

In Situ sALD Setup. A home-built poly(tetrafluoroethylene) (PTFE) flow cell with an inlet and an outlet was used. The PTFE flow cell was pressed with a ring-shaped Kalrez gasket (d = 1.0 mm) against the Si substrate (waver or ATR window). The Kalrez gasket defines the shape and volume of the sALD reaction chamber. The gasket is placed with the PTFE lid on top of the flat side of a hemispherical silicon window. This window served as the ATR window and substrate for the growth of the atomic layer at the same time. The same PTFE and Kalrez equipment was used on a silicon wafer to create an ex situ cell. In this case, the wafer served as the substrate. The PTFE cell was connected with a tubing system (PTFE lines with poly(ether ether ketone) (PEEK) connections) (see Figure 2b). The solutions were pumped (2× precursor, 2× solvents) by four commercial peristaltic pumps (Masterflex C/L Analog Variable-Speed Pump). One precursor tube was connected to one purging solution tube. The lines were joined to one line, which ends in the reaction cell. Pumping rates and times are summarized in Table 1.

For the in situ measurements, the reaction cell was placed with the Si window in the sample compartment of the FT-IR spectrometer (see above). The IR beam was reflected internally toward the detector with an angle of incidence of 60° with respect to the surface normal. The pumps were triggered and the recording of spectra was done separately in an automatized data acquisition procedure.

AFM. Imaging was performed ex situ on a commercial atomic force microscope (Keysight Technologies, Series 5500 AFM/SPM). To minimize the vibrations, a combination of active and passive noise damping was applied. Commercial silicon cantilevers (Opus Otespa) were used with a spring constant of 26 N·m^{-1} and resonance frequency

https://doi.org/10.1021/acsami.2c16943
ACS Appl. Mater. Interfaces 2023, 15, 19536−19544

of 300 kHz. Scanning was performed in intermittent contact mode at scan rates of 0.1−0.5 lines per second. Images were post-processed (data leveling, correct horizontal scars) using the Gwyddion software[44] (version 2.53).

Ellipsometry. Spectroscopic ellipsometry measurements were performed with a SENPro spectroscopic ellipsometer from SENTECH Instruments GmbH. All measurements were performed at an angle of 70° in a spectral range from 370 to 1050 nm. Data analysis was performed with the software SpectraRay3.

Preparation of Si Wafers. Si wafers (Si(100), Si-Mat, $d = 525 \pm 25$ μm, type/dopant: P/Bor) were cleaned in an ultrasonic bath subsequently using the solvents acetone (VWR Chemicals, >99%, technical), isopropanol (VWR Chemicals, >98%, technical), and methanol (VWR Chemicals, >98.5%, technical). Afterward, the surfaces were rinsed with the corresponding solvents and finally dried. The samples were fixed in a home-build ex situ cell (see the Supporting Information for details) and ALD film was deposited following the identical procedure used in the in situ experiments.

Density Functional Theory. DFT calculations were performed using the VASP software v 6.3.0.[45−48] The PBE[49] exchange-correlation functional was used within the projector augmented-wave method (PAW) and a plane wave basis set with an energy cutoff of 450 eV. A Gaussian smearing of 0.005 eV was used as well as the DR-D3[50] correction scheme. The two different structures were optimized until the forces were smaller than 0.001 eV $Å^{-1}$. For these structures, vibrational spectra were calculated by means of numerical gradients displacing each atom in each cardinal direction by 0.02 Å.

Neural Network Approach. The original AFM image was converted into a gray scale image. In the next step, the AFM image was transformed into a vector flow representation.[51] The network characterized the objects and gave characteristic sizes as input. A Python script calling iteratively Cellpose software in combination with ImageJ was developed to determine the particle size distribution from microscopy images. Each iteration optimizes for an increasing seed size but disabling double counting, while checking for double counting and false positives. The procedure was optimized for each sample, regarding background noise and/or the watershed parameters in ImageJ that are used to find the boundaries determined by cellpose and size. The number of iterations depends on the spread of seed sizes in the sample. Within each sample, the analysis parameters were kept constant while analyzing different segments. The particle size distributions were fitted with a log-normal probability distribution on the normalized histograms. The macroscopic surface coverage is obtained by finding the inflection point in area vs threshold intensity curve. The procedure was applied twice (except for images after one cycle), removing in the second iteration cycle typically brighter objects found in the first iteration.

■ RESULTS AND DISCUSSION

A new sALD process was developed to deposit CuSCN on silicon as illustrated in Figure 1a. The sample surface was exposed in alternating manner to the precursors CuOAc (saturated) and LiSCN (saturated) dissolved in $CHCl_3$ (5mL). Between the different precursors, the surface was purged with $CHCl_3$ (36 mL). Note that the final product CuSCN is practically insoluble in many conventional solvents such as chloroform used in this study.[52] By varying the concentration of the precursor CuOAc, we demonstrate that under the conditions applied, the reaction is self-limiting (see the Supporting Information Section 7), which defines the deposition process to be sALD. We propose that the reaction follows an ion exchange mechanism, as illustrated (Figure S5) and discussed in the Supporting Information. For the desired product CuSCN, two phases are reported in the literature.[53] The most common and stable phase is the β-CuSCN wurtzite structure (Figure 1b), with a hexagonal *P63mc* space group, eight atoms (corresponding to two layers of CuSCN) in one unit cell (lattice parameters of $a = b = 3.85$ Å, and $c = 10.94$ Å).[32,54,55] Additionally, CuSCN also exists in a α-CuSCN orthorhombic structure (Figure 1c), with a *Pbca* space group, 32 atoms (corresponding to two layers of CuSCN) in one unit cell (lattice parameters of $a = 7.27$ Å, $b = 6.71$ Å, and $c = 10.94$ Å).[55,56] From ellipsometry measurements, a growth rate of ~1.7 nm per cycle was determined, which is larger than the expected value of 0.6 nm per cycle by a factor of three. We assign the difference to additional coalescence and ripening phenomena, which are discussed below and are responsible for the formation of three-dimensional structures. To study the growth process in detail, a dedicated sALD setup (Figure 2) was developed. It enables to characterize the films deposited on Si wafers by ex situ methods such as ellipsometry, energy dispersive X-ray spectroscopy (EDX), scanning electron microscopy (SEM), and AFM. Moreover, it enables to monitor deposition directly in situ by ATR-IR spectroscopy. For this purpose, the film was directly deposited on a Si ATR window. The experiment consists of four peristaltic pumps for the different precursors and solvents, a PTFE flow cell, and a vacuum-based FT-IR spectrometer with optics for ATR measurements (see Figure 2a). The pumps and the recording of spectra are triggered via an interface in an automatized data acquisition procedure. A detailed description of the experiment is given in the section Experimental and Theoretical Methods and Section 6 of the Supporting Information.

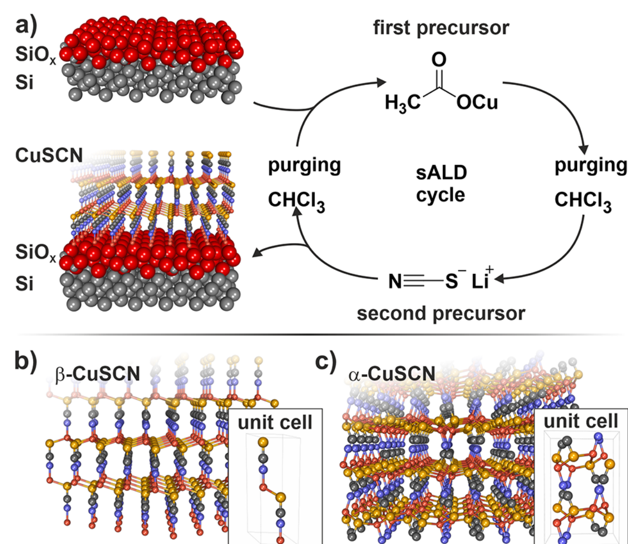

Figure 1. Schematic representation of the sALD process investigated in this work: (a) scheme of one sALD cycle to deposit CuSCN on a silicon substrate; crystal structure and unit cell of (b) β-CuSCN and (c) α-CuSCN; blue = nitrogen, yellow = sulfur, gray = carbon, and red = copper.

For both in situ and ex situ investigations, identical procedures were used as depicted in Figure 2b, optimized for the in situ study. Extended pumping and purging times were used to minimize the impact of the cell design, which has to be compatible with in situ IR spectroscopy. Note that transfer to applications requires upscaling, comprising reoptimization of the applied conditions. To imitate the acquisition time of the IR measurements in the ex situ experiments, corresponding waiting times were implemented in the procedure. Before the measurement, the whole setup was flushed with $CHCl_3$ and subsequently a reference spectrum (acquisition time 6 min 48 s) was recorded. Note that we provide purging times and flow rates in Table 1. A

https://doi.org/10.1021/acsami.2c16943
ACS Appl. Mater. Interfaces 2023, 15, 19536−19544

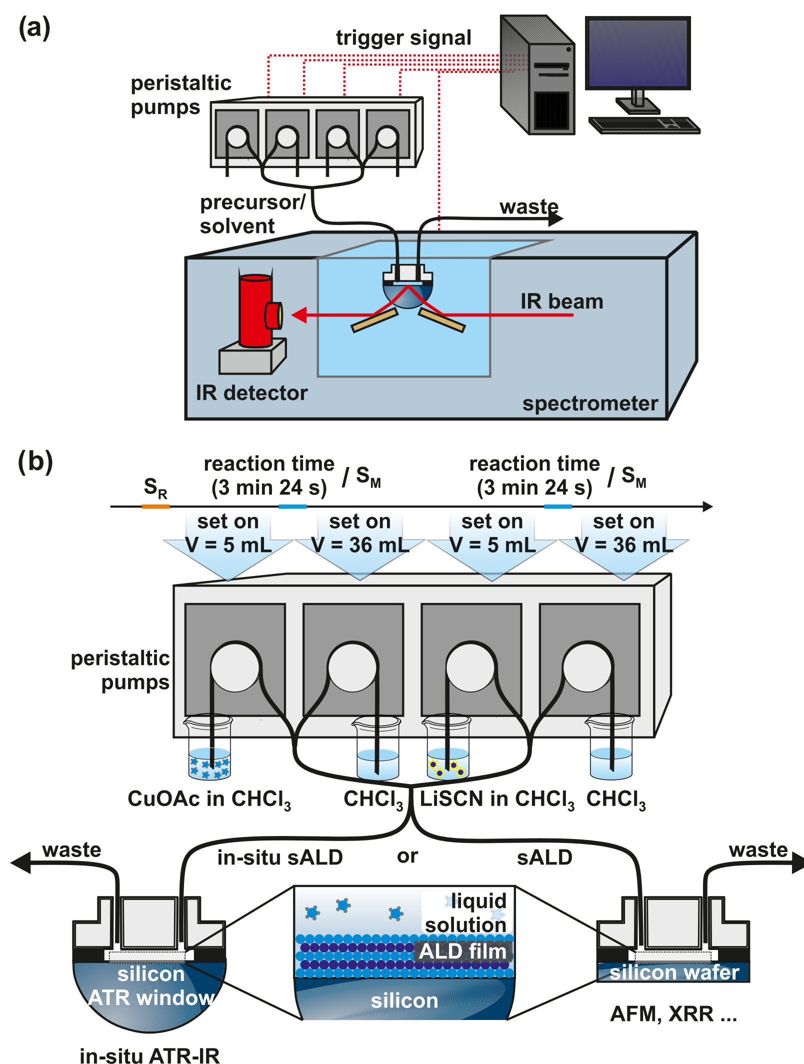

Figure 2. Experimental setup: (a) schematic representation of the sALD cell for in situ and ex situ experiments and (b) schematic representation of the experimental procedure applied. S_R, reference spectrum; S_M, measurement spectrum; sALD, solution atomic layer deposition; ATR-IR, attenuated total reflection infrared; and AFM, atomic force microscopy.

solution of CuOAc (sat.) in $CHCl_3$ was used as the first precursor to cover the surface with a Cu^I layer. After purging the cell, the first IR spectrum in ATR mode (acquisition time 3 min 24 s) was recorded. Then, the cell was rinsed with pure $CHCl_3$ to clean the reaction chamber from the unreacted precursor. Afterward, the second precursor sat. LiSCN in $CHCl_3$ was introduced and a second spectrum was recorded. In the last step, the cell was rinsed with $CHCl_3$.

In the first step, the surface topography was characterized during the CuSCN film growth by ex situ AFM. Images of the pristine Si wafer with a native oxide layer and the Si wafer after 1, 2, 3, 9, 23, and 50 sALD cycles were recorded. Note that separate samples for the different number of cycles were prepared to minimize the influence of contaminations. Images of the Si surface as well as the initial three cycles are shown in Figure 3. AFM images of the pristine Si surface (Figure 3a) show a flat surface without particles. The root mean square value of the surface roughness (R_q) is 121 pm. After the first ALD cycle (Figure 3b), the formation of small hemispherical nanoparticles is observed. A direct comparison with the control experiment, in which only the solvents in the absence of the precursors were purged (see Figure S2 for details), indicates that the particles observed result from the sALD process. Additionally, the surface corrugation changes even for the parts of the surface where no nanoparticles are apparent (see magnification in the inset). In this area, R_q increases to 158 pm, indicating growth of a two-dimensional (2D) surface layer. With increasing cycle number (Figure 3c,d), the particle density increases. A narrow particle size distribution is observed, indicating that no coalescence and/or Ostwald ripening occurs in the initial cycles, and the surface becomes homogeneously covered by nanoparticles. Note that all three observations are in perfect agreement with the initial nucleation found for gas-phase ALD.[57−60] In Figure 4, the growth of the CuSCN film up to 50 cycles is displayed. After nine cycles, the surface coverage further increases and for cycle numbers ≥ 23, agglomeration of the particles to larger clusters is observed, which reach heights of up to 40 and 70 nm for 23 and 50 sALD cycles, respectively. Note that the nanoparticle substructure is still evident. It is generally accepted that many ALD processes occur via an island growth mode forming nanoparticles in the initial cycles.[57−60] This can take place for example when the surface tension is high between the substrate and the grown layer, such as for sulfides or for metals on an oxide surface, which favors to the growth of nanoparticles.[61] The

https://doi.org/10.1021/acsami.2c16943
ACS Appl. Mater. Interfaces 2023, 15, 19536−19544

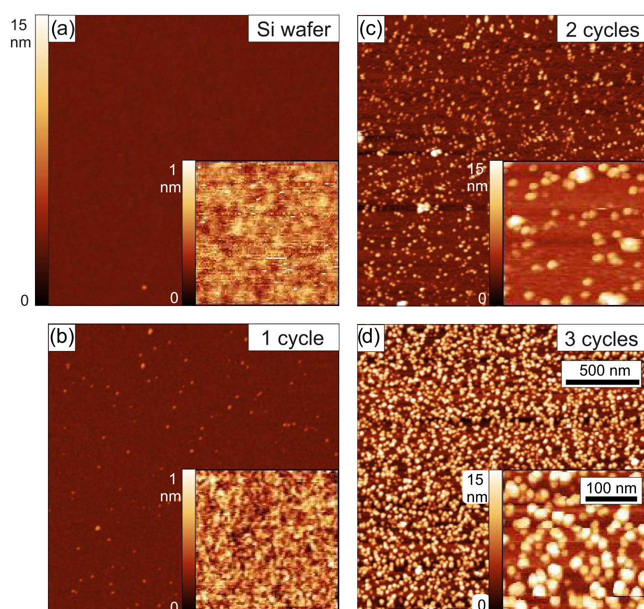

Figure 3. (a−d) AFM images of CuSCN on Si with increasing number of sALD cycles. The color range in all 2 μm × 2 μm images is 15 nm. The scale is identical for all large images and for all insets.

nucleation can be improved by surface pretreatment[62] and/or modifying the substrate. In the case of sALD, it was also demonstrated that the solvent can modify the morphology of the deposited layer and additionally it is possible to use additives to improve the growth behavior.

To quantify the particle size and density, the images were analyzed by a neural network approach. In Figure 5a, the probability is shown as a function of the particle diameter. Note that the absolute values of the particle size in AFM images are generally overestimated due to tip convolution effects.[63] This error is, however, systematic. In the initial cycle, the highest fraction of particles exists with a diameter of 27 nm and a narrow particle size distribution. In the first few cycles, the particles in each window scale with the cycle number such that the distribution does not change significantly while the probability maximum stays at 27 nm. By increasing the number of cycles from 9 to 23 and 50, the particle size distribution broadens to smaller but more drastically larger particles. The broadening of the particle size distribution is assigned to coalescence and Ostwald ripening, which determine the particle size and its distribution in the growth process. Consistently with these findings, the density of particles (Figure 5b) increases for the first three cycles up to 467 particles·μm^{-2}, reaches a plateau at nine cycles, upon which the density decreases at higher cycle numbers to a value of 117 particles·μm^{-2} at 50 cycles. The development of the particle size and size distribution is in line with a model that involves nucleation, growth, coalescence, and/or ripening. These results suggest that nucleation dominates in the first few cycles. The particle density increases but their size distribution stays nearly constant. In later cycles, the particle density reaches a maximum and decreases thereafter, suggesting that the growth of the particle and therefore coalescence and/or Ostwald ripening become more significant.[64] As a result, at 50 cycles, the distribution becomes very broad with finite likelihood of very large clusters of up to 226 nm in effective diameter.

Finally, the sALD process was studied in situ by IR spectroscopy. As a reference, initially, the transmission spectrum of the CuSCN powder (Figure 6a) was measured and compared to the calculated spectra of α-CuSCN and β-CuSCN. In the transmission spectrum, a sharp peak is present at 2175 cm^{-1} with a broad, red-shifted shoulder that is associated with the ν(CN) vibrations. The DFT simulations predict that the bands of the α- and β-phase differ by 24 cm^{-1} and the latter band is shifted to the red. Consequently, the band at 2175 cm^{-1} (blue) is assigned to the β-structure of CuSCN and the shoulder to the less stable α-structure of CuSCN. This assignment is in agreement with previous works.[65−70]

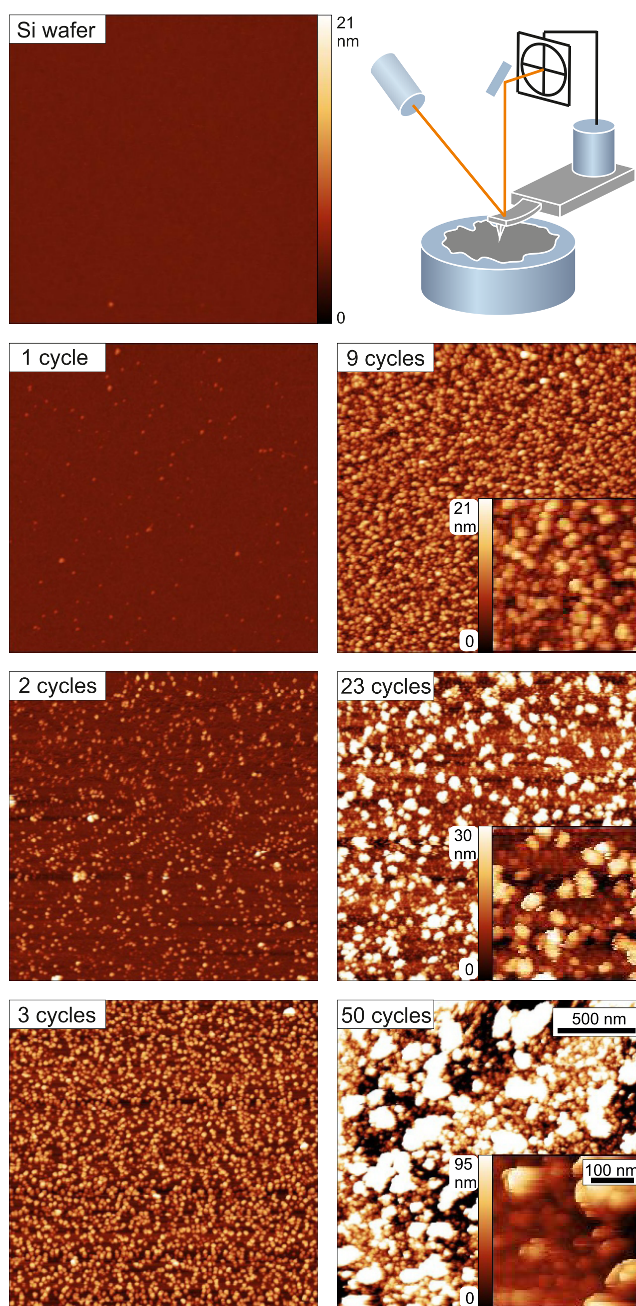

Figure 4. AFM images of CuSCN on Si with increasing number of sALD cycles. The color range in 2 μm × 2 μm images is 21 nm. The scale is identical for all large images and for all insets.

For the in situ measurements, the standard procedure described before (see also Figure 2b) was used. The spectra within one sALD cycle were averaged to improve the signal-to-noise ratio. The resulting ATR-IR spectra in the frequency region of the ν(CN) vibrations are shown in Figure 6b.

https://doi.org/10.1021/acsami.2c16943
ACS Appl. Mater. Interfaces 2023, 15, 19536−19544

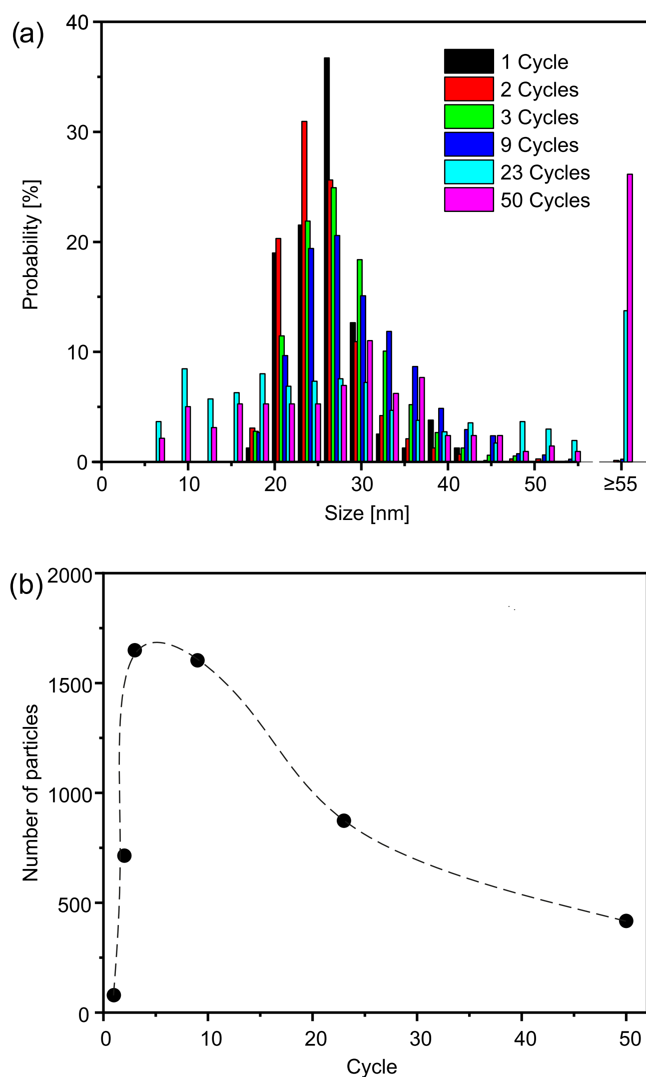

Figure 5. Particle statistics derived from the neural network approach: (a) size distribution histogram of CuSCN nanoparticles as a function of the sALD cycle number and (b) absolute number of particles identified in 2 μm × 2 μm images as a function of cycle number.

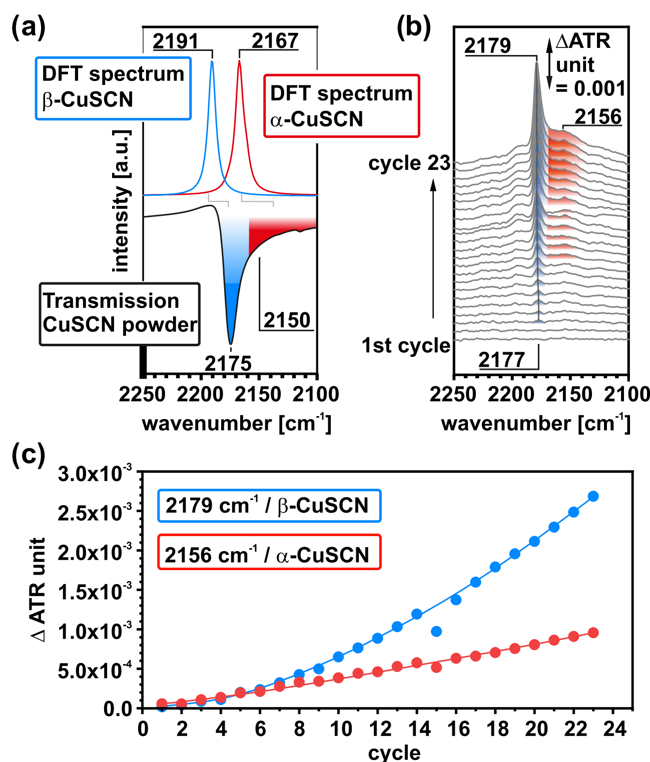

Figure 6. In situ IR spectra recorded during the sALD process: (a) reference DFT spectra of α-CuSCN and β-CuSCN in comparison with the transmission spectrum of the CuSCN powder; (b) ATR-IR spectra recorded during a sALD process comprising 23 full cycles; and (c) peak intensity of the CuSCN bands as a function of the sALD cycle number.

Additionally, the spectra from 3000 to 1100 cm^{-1} are provided in Figure SI1c. Starting from cycle 3, a band develops at 2177 cm^{-1}. With increasing number of sALD cycles, the band increases in intensity and its maximum shifts by about 2 cm^{-1} to the value of 2179 cm^{-1} (see Figure SI3). Together with the band at 2079 cm^{-1}, a red-shifted shoulder at 2156 cm^{-1} is observed, which also increases in intensity with increasing cycle number. This band is very broad in comparison to the other peak. The band at 2177 cm^{-1} indicates the formation of β-CuSCN on the SiO_x/Si surface, which is the most common phase in CuSCN thin films.[31] The increase in band intensity with increasing cycle number demonstrates the film growth with each cycle. The blue shift of the band in the initial cycles is attributed to dipole coupling effects during the formation of small β-CuSCN clusters.

Based on our calculated IR spectra, the shoulder at 2156 cm^{-1}, at least in part, is assigned to the growth of an additional α-CuSCN phase. The band, however, is very broad, which indicates further contributions of defect sites and small aggregates (surface effects) to the band shape.[71] In Figure 6c, the band intensities of α-CuSCN and β-CuSCN are plotted for the different cycle numbers. The band intensities of both phases increase with increasing cycle number, while the band intensity of the β-CuSCN phase becomes more dominant with increasing cycle number. The increase of the total band intensity in the initial cycles, however, is smaller than at later cycles. This development is in good agreement with the structural observation obtained from AFM. While in the initial sALD cycles material deposition is dominated by the nucleation of small aggregates on the two-dimensional support, materials deposition at later ALD cycles is dominated by the growth of large three-dimensional particles, which provide a larger surface for the growth.

■ CONCLUSIONS

A solution atomic layer deposition process was investigated for the first time in situ by IR spectroscopy using a newly developed sALD flow cell. Specifically, a novel sALD process for the controlled deposition of CuSCN on a Si substrate was studied. The study is complemented with ex situ atomic force microscopy and ellipsometry measurements. The experimental data were analyzed by the help of computational methods, namely, density functional theory and a neural network approach. From our observations, we conclude the following.

1. *Solution-based atomic layer deposition of CuSCN*: CuSCN is grown on the Si substrate by an atomic layer process from solution using the precursors CuOAc and LiSCN dissolved in $CHCl_3$.
2. *Ex situ and in situ methods:* the developed experimental approach allows to investigate deposition by ex situ methods, such as AFM, as well as to monitor deposition

https://doi.org/10.1021/acsami.2c16943
ACS Appl. Mater. Interfaces 2023, 15, 19536−19544

by in situ methods such as IR spectroscopy. For the in situ measurements, the sALD film is grown directly on a Si hemisphere, which serves as an attenuated total reflection window.

3. *Morphology of the layer growth*: after the initial sALD cycle, the roughness of the surface increases from 121 to 158 pm, which is assigned to the formation of a two-dimensional layer. Additionally, the nucleation of the first three-dimensional spherical nanoparticles is observed. The density of particles increases within the first three sALD cycles from 22 to 467 particles$\cdot\mu m^{-2}$. In the subsequent cycles, the particle size increases drastically and the particle density decreases. The processes indicate the transition to a region where coalescence and/or Ostwald ripening occur. This leads to a rougher surface and an increased deposition per cycle.
4. *Chemical nature and structure of the deposits during layer growth*: bulk CuSCN is deposited preferentially in the β-CuSCN phase. However, a small fraction of the α-CuSCN phase and defect sites are formed in the initial stages of deposition. The β-CuSCN phase as well as the α-CuSCN phase and defect sites all grow, whereas the β-CuSCN phase becomes more dominant at larger film thickness.

The experimental and theoretical approach presented here provides microscopic insights into the nucleation, growth, and properties of CuSCN deposits formed by the newly developed sALD process. In the particular case of CuSCN grown on silicon wafers, the material is deposited mostly by nucleation of novel particles during the first 10 cycles, after which their growth and coalescence and also Ostwald ripening take over. In the future, similar experimental methods in the development of sALD processes for other materials or on other substrates will be applied, as well. Therefore, it is crucial to understand the growth mechanism and use it to grow materials with a specific morphology on specific substrates.

ASSOCIATED CONTENT

Supporting Information

The Supporting Information is available free of charge at https://pubs.acs.org/doi/10.1021/acsami.2c16943.

In situ IR spectra between 3000 and 1100 cm^{-1} of the growth of CuSCN by sALD; comparison of AFM images of the growth of CuSCN by sALD with the corresponding blind experiments; ν(SCN) band position of ν-CuSCN during 23 cycles of the sALD process; detailed measurement procedure and proposed reaction mechanism for deposition of CuSCN; description of home-build in situ sALD flow cell; and proof of self-limitation of the deposition process (PDF)

AUTHOR INFORMATION

Corresponding Author

Olaf Brummel − *Interface Research and Catalysis, Erlangen Center for Interface Research and Catalysis, Friedrich-Alexander-Universität Erlangen-Nürnberg, 91058 Erlangen, Germany*; orcid.org/0000-0001-5968-0774; Email: olaf.brummel@fau.de

Authors

Felix Hilpert − *Interface Research and Catalysis, Erlangen Center for Interface Research and Catalysis, Friedrich-Alexander-Universität Erlangen-Nürnberg, 91058 Erlangen, Germany*; orcid.org/0000-0002-2765-6451

Pei-Chun Liao − *Chemistry of Thin Film Materials (CTFM), IZNF, Friedrich-Alexander-Universität Erlangen-Nürnberg, 91058 Erlangen, Germany*

Evanie Franz − *Interface Research and Catalysis, Erlangen Center for Interface Research and Catalysis, Friedrich-Alexander-Universität Erlangen-Nürnberg, 91058 Erlangen, Germany*; orcid.org/0000-0002-2070-0050

Vanessa M. Koch − *Chemistry of Thin Film Materials (CTFM), IZNF, Friedrich-Alexander-Universität Erlangen-Nürnberg, 91058 Erlangen, Germany*; orcid.org/0000-0003-4560-787X

Lukas Fromm − *Lehrstuhl für Theoretische Chemie, Friedrich-Alexander-Universität Erlangen-Nürnberg, 91058 Erlangen, Germany*

Ece Topraksal − *PULS Group Physik Department, Friedrich-Alexander-Universität Erlangen-Nürnberg, 91058 Erlangen, Germany; Germany Group for Computational Life Sciences, Division of Physical Chemistry, Ruđer Bošković Institute, 10000 Zagreb, Croatia*

Andreas Görling − *Lehrstuhl für Theoretische Chemie, Friedrich-Alexander-Universität Erlangen-Nürnberg, 91058 Erlangen, Germany*; orcid.org/0000-0002-1831-3318

Ana-Sunčana Smith − *PULS Group Physik Department, Friedrich-Alexander-Universität Erlangen-Nürnberg, 91058 Erlangen, Germany; Germany Group for Computational Life Sciences, Division of Physical Chemistry, Ruđer Bošković Institute, 10000 Zagreb, Croatia*; orcid.org/0000-0002-0835-0086

Maïssa K. S. Barr − *Chemistry of Thin Film Materials (CTFM), IZNF, Friedrich-Alexander-Universität Erlangen-Nürnberg, 91058 Erlangen, Germany*; orcid.org/0000-0003-1587-2269

Julien Bachmann − *Chemistry of Thin Film Materials (CTFM), IZNF, Friedrich-Alexander-Universität Erlangen-Nürnberg, 91058 Erlangen, Germany*; orcid.org/0000-0001-6480-6212

Jörg Libuda − *Interface Research and Catalysis, Erlangen Center for Interface Research and Catalysis, Friedrich-Alexander-Universität Erlangen-Nürnberg, 91058 Erlangen, Germany*; orcid.org/0000-0003-4713-5941

Complete contact information is available at: https://pubs.acs.org/10.1021/acsami.2c16943

Author Contributions

⊥F.H. and P.-C.L. contributed equally to this work.

Notes

The authors declare no competing financial interest.

ACKNOWLEDGMENTS

The authors acknowledge financial support by the Deutsche Forschungsgemeinschaft (DFG) Research Unit FOR 1878 "Functional Molecular Structures on Complex Oxide Surfaces" (Project 214951840) and further projects (Collaborative Research Centre SFB 1452——Catalysis at Liquid Interfaces, Projects 431733372, 453560721, 322419553, 392607742). The authors also acknowledge additional financial support by the German Federal Ministry of Education and Research (BMBF, Project Combined Infrared and X-ray Analytics of Energy Materials, CIXenergy 05K19WE1) and by the Bavarian ministry of Economic Affairs, Regional Development and Energy.

REFERENCES

(1) George, S. M. Atomic Layer Deposition: An Overview. *Chem. Rev.* **2010**, *110*, 111−131.
(2) Johnson, R. W.; Hultqvist, A.; Bent, S. F. A Brief Review of Atomic Layer Deposition: From Fundamentals to Applications. *Mater. Today* **2014**, *17*, 236−246.
(3) Suntola, T.; Antson, J. Method for Producing Compound Thin Films. U.S. Patent US4,058,430A, 1977.
(4) Ahonen, M.; Pessa, M.; Suntola, T. A Study of ZnTe Films Grown on Glass Substrates Using an Atomic Layer Evaporation Method. *Thin Solid Films* **1980**, *65*, 301−307.
(5) Sveshnikova, G. V.; Kol'tsov, S. I.; Aleskovskii, V. B. Formation of a Silica Layer of Predetermined Thickness on Silicon by the Molecular Layering Method. *Zh Prikl Khim* **1970**, *43*, 1150−1152.
(6) Kol'tsov, S. I. Preparation and Investigation of the Products of Interaction between Titanium Tetrachloride and Silica Gel. *J. Appl. Chem. USSR* **1969**, *42*, No. 975.
(7) Sveshnikova, G. V.; Kol'tsov, S. I.; Aleskovskii, V. B. Interaction of Titanium Tetrachloride with Hydroxylated Silicon Surfaces. *J. Appl. Chem. USSR* **1970**, *43*, 432−434.
(8) Kol'tsov, S. I.; Tuz, T. V.; Volkova, A. N. Molecular Layering of Boron Oxide on the Surface of Silica. *J. Appl. Chem. USSR* **1979**, *52*, 2074−2077.
(9) Nechiporenko, A. P.; Sukhareva, T. M.; Malygin, A. A.; Kol'tsov, S. I.; Aleskovskii, V. B. Ultramicrochemical Investigation of Chromium Oxide Layers Synthesized by Molecular Layering on Single-Crystal Germanium and Silicon Surfaces. *J. Appl. Chem. USSR* **1978**, *51*, 2333−2337.
(10) Kol'tsov, S. I.; Kopylov, V. B.; Smirnov, V. M.; Aleskovskii, V. B. Synthesis and Investigation of Aluminum-Oxygen Layers on the Surface of Silica. *J. Appl. Chem. USSR* **1976**, *49*, 525−528.
(11) Kol'tsov, S. I.; Aleskovskii, V. B.; Volkova, A. N.; Smirnov, V. M. Change in the Structure of Silica Gel in the Process of the Formation of a Layer of Phosphorus Pentoxide on Its Surface. *J. Appl. Chem. USSR* **1974**, *47*, 1292−1295.
(12) Zaera, F. The Surface Chemistry of Atomic Layer Depositions of Solid Thin Films. *J. Phys. Chem. Lett.* **2012**, *3*, 1301−1309.
(13) Muñoz-Rojas, D.; Maindron, T.; Esteve, A.; Piallat, F.; Kools, J. C. S.; Decams, J. M. Speeding up the Unique Assets of Atomic Layer Deposition. *Mater. Today Chem.* **2019**, *12*, 96−120.
(14) Nicolau, Y. F. Solution Deposition of Thin Solid Compound Films by a Successive Ionic Layer Adsorption and Reaction Process. *Appl. Surf. Sci.* **1985**, *22−23*, 1061−1074.
(15) Graniel, O.; Puigmartí-luis, J.; Muñoz-Rojas, D. Liquid Atomic Layer Deposition as Emergent Technology for the Fabrication of Thin Films. *Dalton Trans.* **2021**, *50*, 6373−6381.
(16) Cao, Y.; Zhu, S.; Bachmann, J. HfS_2 Thin Films Deposited at Room Temperature by an Emerging Technique, Solution Atomic Layer Deposition. *Dalton Trans.* **2021**, *50*, 13066−13072.
(17) Foong, T. R. B.; Shen, Y.; Hu, X.; Sellinger, A. Template-Directed Liquid ALD Growth of TiO_2 Nanotube Arrays: Properties and Potential in Photovoltaic Devices. *Adv. Funct. Mater.* **2010**, *20*, 1390−1396.
(18) Shen, Y.; Foong, T. R. B.; Hu, X. Towards Atomic Level Vanadium Doping of TiO_2 via Liquid-Phase Atomic Layer Deposition. *Appl. Catal., A* **2011**, *409−410*, 87−90.
(19) Wu, Y.; Döhler, D.; Barr, M.; Oks, E.; Wolf, M.; Santinacci, L.; Bachmann, J. Atomic Layer Deposition from Dissolved Precursors. *Nano Lett.* **2015**, *15*, 6379−6385.
(20) Alam, M.; Miserque, F.; Taguchi, M.; Boulanger, L. J.; Renault, J. P. Tuning Hydrogen Production during Oxide Irradiation through Surface Grafting. *J. Mater. Chem.* **2009**, *19*, 4261−4267.
(21) Le Monnier, B. P.; Wells, F.; Talebkeikhah, F.; Luterbacher, J. S. Atomic Layer Deposition on Dispersed Materials in Liquid Phase by Stoichiometrically Limited Injections. *Adv. Mater.* **2019**, *31*, No. 1904276.
(22) Zankowski, S. P.; Van Hoecke, L.; Mattelaer, F.; De Raedt, M.; Richard, O.; Detavernier, C.; Vereecken, P. M. Redox Layer Deposition of Thin Films of MnO_2 on Nanostructured Substrates from Aqueous Solutions. *Chem. Mater.* **2019**, *31*, 4805−4816.
(23) Taniguchi, A.; Taniguchi, T.; Wagata, H.; Katsumata, K.; Okada, K.; Matsushita, N. Liquid-Phase Atomic Layer Deposition of Crystalline Hematite without Post-Growth Annealing. *CrystEngComm* **2019**, *21*, 4184−4191.
(24) Fichtner, J.; Wu, Y.; Hitzenberger, J.; Drewello, T.; Bachmann, J. Molecular Layer Deposition from Dissolved Precursors. *ECS J. Solid State Sci. Technol.* **2017**, *6*, No. N171.
(25) Ichinose, I.; Hiroyuki, S.; Toyoki, K. Stepwise Adsorption of Metal Alkoxides on Hydrolyzed Surfaces: A Surface Sol-Gel Process. *Chem. Lett.* **1996**, *25*, 831−832.
(26) Kee, Y.; Put, B.; Bardé, F.; Vereecken, P. M. Amorphous MnO_2 Coated 3D Ni Nanomesh as a Thin-Film Hybrid Cathode Material under O_2 Atmosphere. *J. Electrochem. Soc.* **2020**, *167*, No. 020507.
(27) Gregory, B. W.; Stickney, J. L. Electrochemical Atomic Layer Epitaxy (ECALE). *J. Electroanal. Chem. Interfacial Electrochem.* **1991**, *300*, 543−561.
(28) Zhu, W.; Liu, X.; Liu, H.; Tong, D.; Yang, J.; Peng, J. Coaxial Heterogeneous Structure of TiO_2 Nanotube Arrays with CdS as a Superthin Coating Synthesized via Modified Electrochemical Atomic Layer Deposition. *J. Am. Chem. Soc.* **2010**, *132*, 12619−12626.
(29) Stickney, J. L. The Chalkboard: Electrochemical Atomic Layer Deposition. *Electrochem. Soc. Interface* **2011**, *20*, 28−30.
(30) Ledina, M.; Liang, X.; Kim, Y.-G.; Jung, J.; Perdue, B.; Tsang, C.; Soriaga, M.; Stickney, J. L. Investigations into the Formation of Germanene Using Electrochemical Atomic Layer Deposition (E-ALD). *ECS Trans.* **2015**, *66*, 129−140.
(31) Wijeyasinghe, N.; Anthopoulos, T. D. Copper(I) Thiocyanate (CuSCN) as a Hole-Transport Material for Large-Area Opto/Electronics. *Semicond. Sci. Technol.* **2015**, *30*, No. 104002.
(32) Jaffe, J. E.; Kaspar, T. C.; Droubay, T. C.; Varga, T.; Bowden, M. E.; Exarhos, G. J. Electronic and Defect Structures of CuSCN. *J. Phys. Chem. C* **2010**, *114*, 9111−9117.
(33) Subbiah, A. S.; Halder, A.; Ghosh, S.; Mahuli, N.; Hodes, G.; Sarkar, S. K. Inorganic Hole Conducting Layers for Perovskite-Based Solar Cells. *J. Phys. Chem. Lett.* **2014**, *5*, 1748−1753.
(34) Jung, J. W.; Chueh, C.-C.; Jen, A. K.-Y. High-Performance Semitransparent Perovskite Solar Cells with 10% Power Conversion Efficiency and 25% Average Visible Transmittance Based on Transparent CuSCN as the Hole-Transporting Material. *Adv. Energy Mater.* **2015**, *5*, No. 1500486.
(35) Arora, N.; Dar, M. I.; Hinderhofer, A.; Pellet, N.; Schreiber, F.; Zakeeruddin, S. M.; Grätzel, M. Perovskite Solar Cells with CuSCN Hole Extraction Layers Yield Stabilized Efficiencies Greater than 20%. *Science* **2017**, *358*, 768−771.
(36) Petti, L.; Pattanasattayavong, P.; Lin, Y. H.; Münzenrieder, N.; Cantarella, G.; Yaacobi-Gross, N.; Yan, F.; Tröster, G.; Anthopoulos, T. D. Solution-Processed p-Type Copper(I) Thiocyanate (CuSCN) for Low-Voltage Flexible Thin-Film Transistors and Integrated Inverter Circuits. *Appl. Phys. Lett.* **2017**, *110*, No. 113504.
(37) Koch, V. M.; Barr, M. K. S.; Büttner, P.; Mínguez-Bacho, I.; Döhler, D.; Winzer, B.; Reinhardt, E.; Segets, D.; Bachmann, J. A Solution-Based ALD Route towards $(CH_3NH_3)(PbI_3)$ Perovskite: Via Lead Sulfide Films. *J. Mater. Chem. A* **2019**, *7*, 25112−25119.
(38) Bernal Ramos, K.; Clavel, G.; Marichy, C.; Cabrera, W.; Pinna, N.; Chabal, Y. J. In Situ Infrared Spectroscopic Study of Atomic Layer-Deposited TiO_2 Thin Films by Nonaqueous Routes. *Chem. Mater.* **2013**, *25*, 1706−1712.
(39) King, D. M.; Spencer, J. A.; Liang, X.; Hakim, L. F.; Weimer, A. W. Atomic Layer Deposition on Particles Using a Fluidized Bed Reactor with in Situ Mass Spectrometry. *Surf. Coat. Technol.* **2007**, *201*, 9163−9171.
(40) Tallarida, M.; Schmeisser, D. In Situ ALD Experiments with Synchrotron Radiation Photoelectron Spectroscopy. *Semicond. Sci. Technol.* **2012**, *27*, No. 074010.
(41) Van Hao, B.; Groenland, A. W.; Aarnink, A. A. I.; Wolters, R. A. M.; Schmitz, J.; Kovalgin, A. Growth Kinetics and Oxidation

Mechanism of ALD TiN Thin Films Monitored by In Situ Spectroscopic Ellipsometry. *J. Electrochem. Soc.* **2011**, *158*, H214.
(42) Knapas, K.; Ritala, M. In Situ Studies on Reaction Mechanisms in Atomic Layer Deposition. *Crit. Rev. Solid State Mater. Sci.* **2013**, *38*, 167−202.
(43) Sheridan, L. B.; Kim, Y.; Perdue, B. R.; Jagannathan, K.; Stickney, J. L.; Robinson, D. B. Hydrogen Adsorption, Absorption, and Desorption at Palladium Nanofilms Formed on Au(111) by Electrochemical Atomic Layer Deposition (E-ALD): Studies Using Voltammetry and In Situ Scanning Tunneling Microscopy. *J. Phys. Chem. C* **2013**, *117*, 15728−15740.
(44) Nečas, D.; Klapetek, P. Gwyddion: An Open-Source Software for SPM Data Analysis. *Open Phys.* **2012**, *10*, 181−188.
(45) Kresse, G.; Hafner, J. Ab Initio Molecular Dynamics for Liquid Metals. *Phys. Rev. B* **1993**, *47*, 558−561.
(46) Kresse, G.; Furthmüller, J. Efficiency of Ab-Initio Total Energy Calculations for Metals and Semiconductors Using a Plane-Wave Basis Set. *Comput. Mater. Sci.* **1996**, *6*, 15−50.
(47) Kresse, G.; Furthmüller, J. Efficient Iterative Schemes for Ab Initio Total-Energy Calculations Using a Plane-Wave Basis Set. *Phys. Rev. B* **1996**, *54*, 11169−11186.
(48) Kresse, G.; Joubert, D. From Ultrasoft Pseudopotentials to the Projector Augmented-Wave Method. *Phys. Rev. B* **1999**, *59*, No. 1758.
(49) Perdew, J. P.; Burke, K.; Ernzerhof, M. Generalized Gradient Approximation Made Simple. *Phys. Rev. Lett.* **1996**, *77*, 3865−3868.
(50) Grimme, S.; Antony, J.; Ehrlich, S.; Krieg, H. A Consistent and Accurate Ab Initio Parametrization of Density Functional Dispersion Correction (DFT-D) for the 94 Elements H-Pu. *J. Chem. Phys.* **2010**, *132*, No. 154104.
(51) Stringer, C.; Wang, T.; Michaelos, M.; Pachitariu, M. Cellpose: A Generalist Algorithm for Cellular Segmentation. *Nat. Methods* **2021**, *18*, 100−106.
(52) Chaudhary, N.; Chaudhary, R.; Kesari, J. P.; Patra, A.; Chand, S. Copper Thiocyanate (CuSCN): An Efficient Solution-Processable Hole Transporting Layer in Organic Solar Cells. *J. Mater. Chem. C* **2015**, *3*, 11886−11892.
(53) Pattanasattayavong, P.; Promarak, V.; Anthopoulos, T. D. Electronic Properties of Copper (I) Thiocyanate (CuSCN). *Adv. Electron. Mater.* **2017**, *3*, No. 1600378.
(54) Ji, W.; Yue, G.-Q.; Ke, F.-S.; Wu, S.; Zhao, H.-B.; Chen, L.-Y.; Wang, S.-Y.; Jia, Y. Electronic Structures and Optical Properties of CuSCN with Cu Vacancies. *J. Korean Phys. Soc.* **2012**, *60*, 1253−1257.
(55) Shen, Y.; Wang, F. Q.; Wang, Q. Ultralow Thermal Conductivity and Negative Thermal Expansion of CuSCN. *Nano Energy* **2020**, *73*, No. 104822.
(56) Kabešová, M.; Dunaj-jurčo, M.; Serator, M.; Gažo, J.; Garaj, J. The Crystal Structure of Copper(I) Thiocyanate and Its Relation to the Crystal Structure of Copper(II) Diammine Dithiocyanate Complex. *Inorg. Chim. Acta* **1976**, *17*, 161−165.
(57) Puurunen, R. L. Surface Chemistry of Atomic Layer Deposition: A Case Study for the Trimethylaluminum/Water Process. *J. Appl. Phys.* **2005**, *97*, No. 121301.
(58) Baji, Z.; Lábadi, Z.; Horváth, Z. E.; Molnár, G.; Volk, J.; Bársony, I.; Barna, P. Nucleation and Growth Modes of ALD ZnO. *Cryst. Growth Des.* **2012**, *12*, 5615−5620.
(59) Zhao, R.; Wang, X. Initial Growth and Agglomeration during Atomic Layer Deposition of Nickel Sulfide. *Chem. Mater.* **2019**, *31*, 445−453.
(60) Bakke, J. R.; Jung, H. J.; Tanskanen, J. T.; Sinclair, R.; Bent, S. F. Atomic Layer Deposition of CdS Films. *Chem. Mater.* **2010**, *22*, 4669−4678.
(61) Büttner, P.; Scheler, F.; Pointer, C.; Döhler, D.; Barr, M. K. S.; Koroleva, A.; Pankin, D.; Hatada, R.; Flege, S.; Manshina, A.; Young, E. R.; Minguez-Bacho, I.; Bachmann, J. Adjusting Interfacial Chemistry and Electronic Properties of Photovoltaics Based on a Highly Pure Sb_2S_3 Absorber by Atomic Layer Deposition. *ACS Appl. Energy Mater.* **2019**, *2*, 8747−8756.
(62) De Paula, C.; Richey, N. E.; Zeng, L.; Bent, S. F. Mechanistic Study of Nucleation Enhancement in Atomic Layer Deposition by Pretreatment with Small Organometallic Molecules. *Chem. Mater.* **2020**, *32*, 315−325.
(63) Keller, D. Reconstruction of STM and AFM Images Distorted by Finite-Size Tips. *Surf. Sci.* **1991**, *253*, 353−364.
(64) Ostwald, W. Studien über die Bildung und Umwandlung fester Körper. *Z. Phys. Chem.* **1897**, *22U*, 289−330.
(65) Tennakone, K.; Jayatissa, A. H.; Fernando, C. A. N.; Wickramanayake, S.; Punchihewa, S.; Weerasena, L. K.; Premasiri, W. D. R. Semiconducting and Photoelectrochemical Properties of n- and p-Type β-CuCNS. *Phys. Status Solidi (a)* **1987**, *103*, 491−497.
(66) Barthel, J.; Buchner, R.; Wismeth, E. FTIR Spectroscopy of Ion Solvation of $LiClO_4$ and LiSCN in Acetonitrile, Benzonitrile, and Propylene Carbonate. *J. Solution Chem.* **2000**, *29*, 937−954.
(67) Fernando, C. A. N. Kinetics of Photocurrent Generation and Quantum Efficiency of a Resonant Energy Transfer Dye Sensitized Solid State Photovoltaic Cell Made from p-CuCNS and n-SnO_2 Transparent Films on Glass. *Sol. Energy Mater. Sol. Cells* **1993**, *30*, 211−220.
(68) Bowmaker, G. A.; Hanna, J. V.; Hart, R. D.; Healy, P. C.; King, S. P.; Marchetti, F.; Pettinari, C.; Skelton, B. W.; Tabacaru, A.; White, A. H. Mechanochemical and Solution Synthesis, X-Ray Structure and IR and 31P Solid State NMR Spectroscopic Studies of Copper(I) Thiocyanate Adducts with Bulky Monodentate Tertiary Phosphine Ligands. *Dalton Trans.* **2012**, *41*, 7513−7525.
(69) Samarakoon, S. P. A. U. K.; Karunarathna, P. G. D. C. K.; Fernando, C. A. N. Characterization of Fe Doped n-CuSCN/p-Cu_2S Solid-State Photovoltaic Cell. *Mater. Res. Express* **2018**, *5*, No. 065052.
(70) Bowmaker, G. A.; Hanna, J. V. IR Spectroscopy of Two Polymorphs of Copper(I) Thiocyanate and of Complexes of Copper(I) Thiocyanate with Thiourea and Ethylenethiourea. *Z. Naturforsch., B* **2009**, *64*, 1478−1486.
(71) Banerjee, A. Investigation of the Crystallinity of the Modifications of Silica by their IR-Reflectance Spectra. *Z. Naturforsch., A* **1993**, *48a*, 741−742.

Recommended by ACS

Tunable Sulfur Incorporation into Atomic Layer Deposition Films Using Solution Anion Exchange

Julia D. Lenef, Neil P. Dasgupta, *et al.*

MARCH 17, 2023
CHEMISTRY OF MATERIALS

READ

Study on Room-Temperature Wet Oxidation of Silicon Catalyzed by Copper

Xianhui Liu, Shaozhou Li, *et al.*

JANUARY 03, 2023
LANGMUIR

READ

Atom-Scale Chemistry in Chalcopyrite-Based Photovoltaic Materials Visualized by Atom Probe Tomography

Kihwan Kim, Jihye Gwak, *et al.*

NOVEMBER 08, 2022
ACS APPLIED MATERIALS & INTERFACES

READ

A Two-Step Magnetron Sputtering Approach for the Synthesis of Cu_2ZnSnS_4 Films from Cu_2SnS_3\ZnS Stacks

Mohamed Yassine Zaki, Aurelian-Catalin Galca, *et al.*

JUNE 27, 2022
ACS OMEGA

READ

Get More Suggestions >